

# EFFECT OF LOADING PROTOCOL ON HYSTERETIC RESPONSE AND STIFFNESS DETERIORATION OF STEEL HOLLOW STRUCTURAL SECTION COLUMNS

Itsuki MATSUMOTO<sup>1</sup>, Kazuya MITSU<sup>2</sup>, and Kikuo IKARASHI<sup>3</sup>

## SUMMARY

This study investigate the effects of member geometry and loading protocol on the plastic deformation capacity and the hysteretic response of welded box-sections made of 550 N/mm<sup>2</sup> high-strength steel. Static cyclic loading tests, including the monotonic test, are conducted by varying the width-to-thickness ratio to clarify the effects on the ultimate strength and the hysteretic response. The characteristics of the strength deterioration are reported for each load protocol and specimen combination, and qualitative trends are identified in relation to the results under monotonic loading. Furthermore, prior to future complementary studies, finite element method (FEM) numerical analysis is performed to simulate the test results for several material constitutive models including the Chaboche model and the Subloading surface model, and the accuracy is verified. The full-scale test results show that whether or not the loading amplitude exceeds the rotation at the ultimate strength in monotonic loading affects the occurrence of local buckling and that this has a certain correspondence with the strength deterioration behavior. Simulation analysis of the experiment with FEM confirm that the application of combined hardening law with nonlinear kinematic hardening, such as the Chaboche model or the Subloading surface model is valid to accurately simulate the test results under cyclic loading.

**Keywords:** *High-Strength Steel, Welded box-section member, Loading protocol, Plastic deformation capacity, Hysteretic response*

## INTRODUCTION

As exemplified by the Kumamoto earthquake (2016) and Tohoku earthquake (2011), in recent years, earthquakes that include multiple destructive shaking at short intervals have been observed in Japan. Since it is impossible to restore or repair buildings during such earthquakes, essential buildings are required to have a structural design that can withstand multiple destructive earthquakes. On the other hand, the current seismic design method in Japan does not assume the case where extremely rare earthquake occurs multiple times, and the relationship between cyclic seismic response and the behavior of the structural member during the collapse of a structure has not been fully clarified. In steel structural frames, buckling of members and rupture of joints are the main causes of their collapse. This paper focuses on the buckling of box-section members, which are often used as a column, and investigates the ultimate strength and strength deterioration behavior through structural tests and finite element method (FEM) numerical analysis. Numerous studies have been conducted on the strength deterioration behavior of box-section members of steel frames under cyclic loading. Tsuda and Matsui et al. (1998) conducted bending tests on box-section cantilever column members subjected to constant axial compressive and horizontal forces, and an evaluation method of the ultimate strength is shown and the relationship between the deterioration of strength and the width-to-thickness ratio index is verified. Kurata et al. (2005) conducted cyclic loading tests up to 0.1 rad of rotation on box-section members subjected to axial compressive forces and investigated the relationship between the strength deterioration characteristics and the width-to-thickness ratio index in the large deformation region. Yamada and Ishida et al. (2012) used the result of cyclic loading tests to propose an extended

---

<sup>1</sup> Presenter, Graduate student of Arch. and Build. Eng., Tokyo Institute of Technology

<sup>2</sup> Assistant Professor, Dept. of Arch. and Build. Eng., Tokyo Institute of Technology, Dr. Eng.

<sup>3</sup> Professor, Dept. of Arch. and Build. Eng., Tokyo Institute of Technology, Dr.Eng.

skeleton curve that includes the strength deterioration region after the ultimate strength. Sato and Ikarashi et al. (2017) derived the elastic local buckling strength of box-section members, which varies depending on the member geometry and stress state by theoretical analysis based on the energy method. Based on this, an index for the new width-to-thickness ratio scale,  $S_h$ , is proposed that considers member geometry and stress state, and a method is devised to evaluate the structural performance of box-section members subjected to cyclic loading using  $S_h$ . Sato et al. (2017) classified the collapse modes that occur in cold-formed box-section members subjected to constant axial compressive forces and cyclic one-end bending moments and analyzed the correspondence with the design formulae for columns given in the *Recommendation for Limit State Design of Steel Structures* (by Architectural Institute of Japan, 2010). Koetaka et al. (2018) conducted experiments and finite element method numerical analyses on cold-pressed box-section members to investigate the effects of member geometry and stress state on two types of collapse state, local buckling and ductile fracture, and find a trend in the parameters that would lead to the precedence of ductile fracture. In addition to the above, researches on numerical analytical models that simulate hysteresis characteristics in the strength deterioration region has been conducted vigorously, and modeling methods such as fiber models and multi-spring models have been proposed.

The deterioration behavior of members is considered to be affected not only by the member geometry (e.g. width-to-thickness ratio) and stress state (e.g. presence or absence of axial force), but also by the loading protocol. Several experiments focusing on the loading protocol have been carried out so far, giving different loading protocols to specimens of the same geometry, and Suzuki et al. (2021) pointed out that similar fracture modes occur regardless of the loading protocol. However, the relationship between loading protocol and structural performance such as ultimate strength and strength deterioration behavior has not been fully clarified.

Since conducting a comprehensive test combining member geometry and loading protocols through experiments is not practical, complementary studies are being conducted using the finite element method (FEM) numerical analysis. When cyclic loading experiments are simulated by the FEM, it is important to apply a material constitutive model that can simulate material nonlinearity with high accuracy, since it greatly affects the results. In numerous studies, the linear kinematic hardening rule or the combined hardening rule with isotropic hardening is often adopted to FEM analysis. This is intended to ensure the consistency of the Bauschinger part among the load-displacement relationships obtained from the experiment. In recent years, material constitutive models such as the Chaboche model (1983), which expresses the hardening properties as a superposition of nonlinear kinematic hardening laws, the Y-U model (2003), and the Subloading surface model (1989) have been proposed to simulate the material nonlinearity of steel in more detail. In particular, the Chaboche model has already been used in FEM analysis in previous studies due to its clear expression and the few parameters that need to be calibrated, and some methods for calibrating material parameters have also been proposed.

Based on these background, the purpose of this study is to clarify the effect of cyclic loading protocol on structural performance determined by local buckling by means of structural experiments. Since it is impossible to perform structural experiments exhaustively, this study also examines the applicability of FEM analysis. An methods for applying the constitutive models to FEM analysis of steel structural members are proposed, and several models are applied to simulate structural experiments to verify the accuracy of each model.

## **CYCLIC BENDING SHEAR TESTS OF WELDED BOX-SECTION MEMBER**

### **Test specimen overview**

Table 1 lists the parameters and symbols used in this paper. In this study, welded box-section member is selected as the test specimen, and each member is made of 550N/mm<sup>2</sup> (Gr.55) grade steel. Table 2 summarizes the coupon test results. Cross-sections of each column are □-125x4.5, □-110x3.2, and □-125x3.2 as shown in Table 3. The width-to-thickness ratio of each specimen is 27.8, 34.5, and 39.1, which is the value at which local buckling is expected to occur prior to ductile crack under cyclic loading. In addition, as shown in Fig. 1, no backing plate is used for welding assembly, and full penetration welding is applied to the groove on the web side. This is to eliminate the restraining effect of the plate component by the backing plate, and similarly, no backing plate is used at the welds to the end plates. The shear span from the surface of the end plate to the loading position is 553 mm for each specimen.

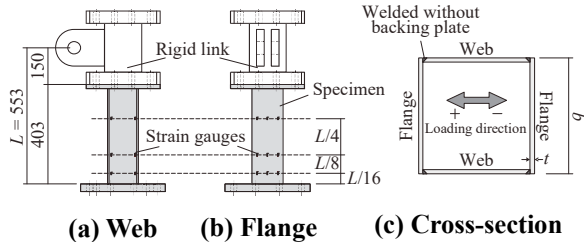
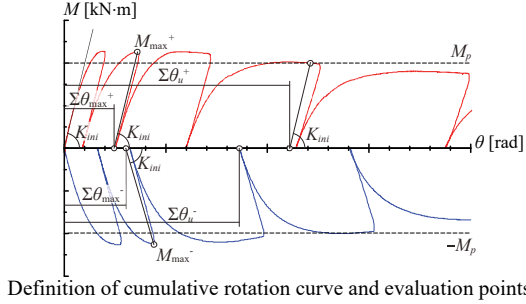
### **Test equipment and measurement plan**

Fig. 2 shows the overview of the test set-up. The horizontal force is applied to the top of the specimen via a rigid jig. Out-of-plane deformation is restrained by horizontal braces. Specimens are placed so that the welding line form on the web side. As shown in Fig. 1, strain gauges are attached in three layers along the length direction to

enable measurement of local plate deformation and stress distribution. As shown in Fig. 2, the displacement transducers measure the horizontal and vertical displacement of the column top, the horizontal displacement of the end plate, and the rotation of the end plate. The rotation  $\theta$  is calculated from these measurement results. The horizontal load is measured by a load cell connected to an oil jack supported by a pin at both ends.

**Table 1 Parameters and symbols**

$b$ : Flange width [mm]	
$E_m$ : Modulus of elasticity [N/mm <sup>2</sup> ]	
$t$ : Thickness [mm]	
$\nu$ : Poisson's ratio [-]	
$L$ : Shear span [mm]	
$\sigma_{y,m}$ : Yield point [N/mm <sup>2</sup> ]	
$Z$ : Section modulus [mm <sup>3</sup> ]	
$\sigma_{u,m}$ : Tensile Strength [N/mm <sup>2</sup> ]	
$Z_p$ : Plastic section modulus [mm <sup>3</sup> ]	
$Y.R.$ : Yield ratio [%] ( $= \sigma_{y,m}/\sigma_{u,m} \times 100$ )	
$S_H$ : Index for width-to-thickness ratio	$E_{long}$ : Elongation [%]
$M_p$ : Plastic bending moment [kN·m]	$\theta_p$ : Elastic rotation at $M_p$ [rad]
$M_{max}^+$ : Maximum bending moment at the positive loading direction [kN.m]	
$M_{max}^-$ : Maximum bending moment at the negative loading direction [kN.m]	
$\theta_{max}^+$ : Plastic rotation until $M_{max}^+$ [rad]	$\theta_u^+$ : Plastic rotation until $M_p^+$ [rad]
$\Sigma\theta_{max}^+$ : Cumulative rotation until $M_{max}^+$ [rad]	$\Sigma\theta_u^+$ : Cumulative rotation until $M_p^+$ [rad]
$\Sigma\theta_{max}^-$ : Cumulative rotation until $M_{max}^-$ [rad]	$\Sigma\theta_u^-$ : Cumulative rotation until $M_p^-$ [rad]



**Figure 1 Test specimen, construction detail, and strain gauge layout**

**Table 2 Measured material properties of Gr. 55**

$t$	$E_m$	$\sigma_{y,m}$	$\sigma_{u,m}$	$Y.R.$	$E_{long}$
3.2	204000	488.9	584.8	83.6	27.4
4.5	199000	497.1	577.5	83.2	27.6

**Table 3 Geometric parameters**

No.	Size	$b$	$t$	$b/t$	$L$	$L/b$	$M_p$	$\theta_p$	$S_H$
No. 1	□-125×4.5	125	4.5	27.8	553	4.42	48.7	0.0094	0.56
No. 2	□-110×3.2	110	3.2	34.4	553	5.03	26.8	0.0100	0.69
No. 3	□-125×3.2	125	3.2	39.1	553	4.42	34.8	0.0090	0.77

## Cyclic loading protocol

Fig. 3 shows the loading protocol (L.P.) used in the experiment. The protocols are classified into monotonic loading shown in Fig. 3(a), symmetric cyclic loading shown in Fig. 3(b)–(d), and asymmetric cyclic loading shown in Fig. 3(e), (f). Fig.3(b) is a symmetrical loading protocol (L.P.: S.I.1) in which, with the elastic rotation  $\theta_p$  at the full plastic moment as the reference, the even multiples of  $\theta_p$  are repeated twice, positive and negative. Therefore, the member experiences amplitude with plasticization from the initial cycle. Fig. 3(c) is the same symmetrical positive-negative alternating cyclic loading protocol (L.P.: S.I.2) but includes the loop from the elastic to the plastic range to follow the continuous change in structural performance. This protocol is controlled by the rotation  $\theta$ , which is not normalized by  $\theta_p$ . Fig. 3(d) shows a symmetrical loading protocol of constant amplitude (L.P.: S.C.), which is intended to simulate the response due to long-period ground motion. In this study, in order to reach the plasticity region in any case, 0.015 rad (Corresponding to  $1.5\theta_p$ ) is the minimum (L.P.: S.C.3), and 0.02 rad (L.P.: S.C.2) and 0.03 rad (L.P.: S.C.1) are applied as amplitudes. Fig. 3(e), which has an asymmetric protocol, is the Near-Fault loading protocol (L.P.: N.F.) set up to confirm the effect of pulsed seismic motion near a fault on structural performance. This is adopted for the purpose of confirming the structural performance when residual deformation is accumulated in one direction. Fig. 3(f) is a Ratcheting-type loading protocol (L.P.: R.), which assumes the building deformation develops in one direction during a huge earthquake, similar to the Near-Fault type. As shown in Table 4, experiments are carried out on a total of 17 specimens that combined the member geometry and loading protocols.

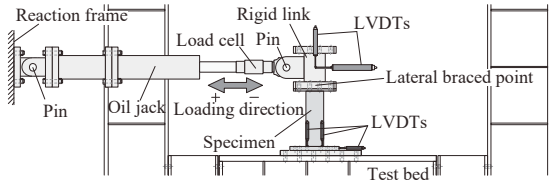


Figure 2 Set-up for experimental test

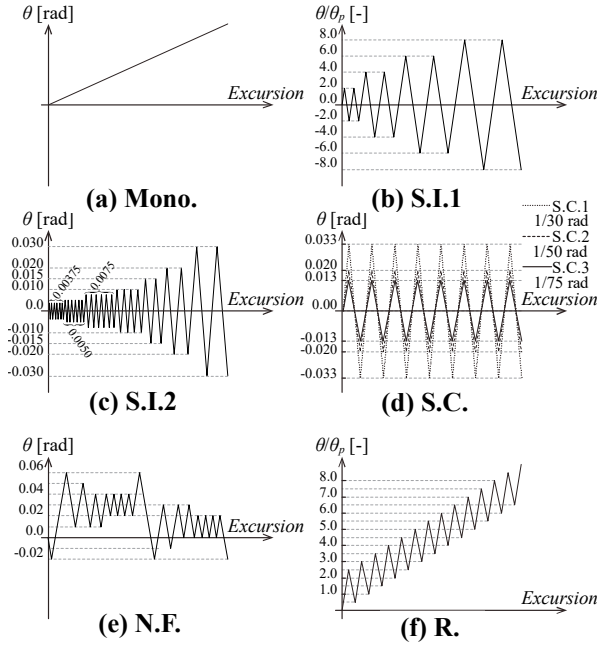


Figure 3 Loading Protocols (L.P.)

Table 4 Matrix of loading protocols

L.P.	Mono.	Symmetrical					Asymmetrical	
		S.I.1	S.I.2	S.C.1 (0.033 rad)	S.C.2 (0.020 rad)	S.C.3 (0.015 rad)	N.F.	R.
No. 1	○	○	○	○	○	○	○	○
No. 2	○	○	○			○		
No. 3	○	○	○		○	○	○	

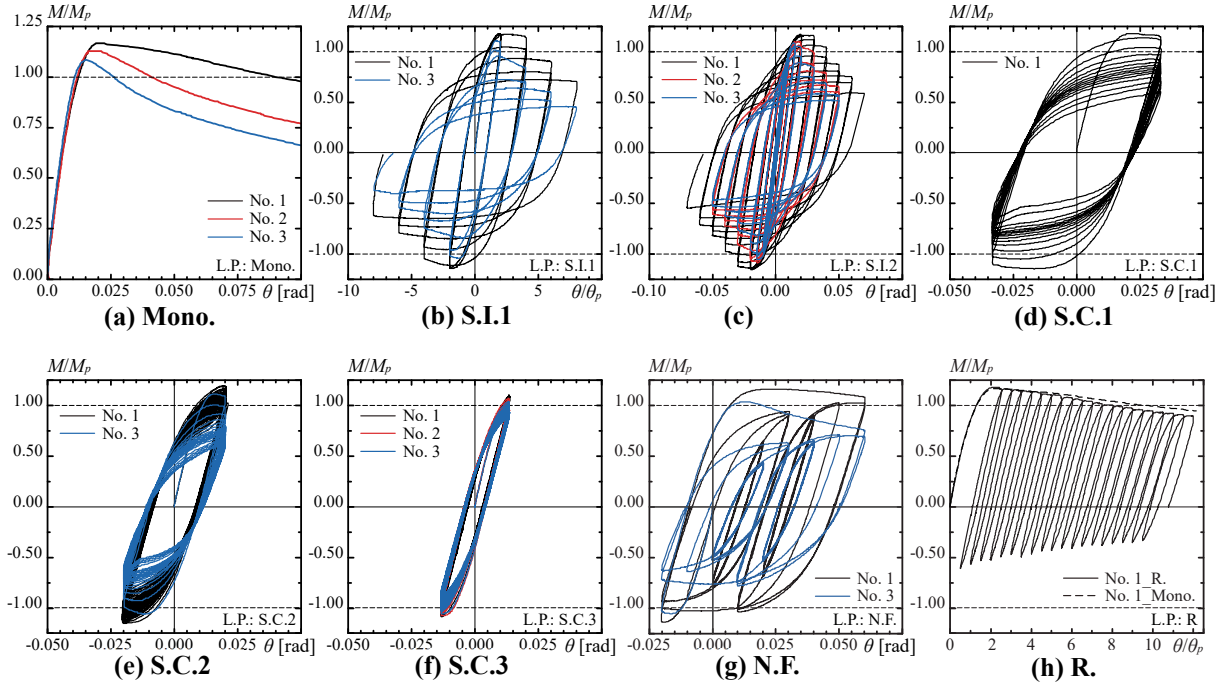
Table 5 Summary of the test result

No.	L.P.	$M_{max}^+$	$M_{max}^-$	$\theta_{max}$	$\theta_u$	$\Sigma\theta_{max}^+$	$\Sigma\theta_{max}^-$	$\Sigma\theta_u^+$	$\Sigma\theta_u^-$
No. 1	Mono.	57.1	-	0.0239	0.0720	-	-	-	-
	S.I.1	57.6	-55.6	-	-	0.0183	0.0257	0.1261	0.0868
	S.I.2	56.9	-56.2	-	-	0.0553	0.0634	0.167	0.196
	C.A.1	57.3	-56.0	-	-	0.0249	0.0393	0.105	0.0840
	C.A.2	58.4	-56.1	-	-	0.0191	0.0273	0.559	0.318
	C.A.3	53.9	-53.1	-	-	0.0196	0.0167	0	0.210
	N.F.	56.6	-55.7	-	-	0.0357	0.0188	0.0742	0.0621
	R.	57.5	-29.7	-	-	0.0213	-	0.104	-
No. 2	Mono.	30.5	-	0.0192	0.0313	-	-	-	-
	S.I.2	29.7	-29.4	-	-	0.0407	0.0445	0.107	0.0777
	C.A.3	29.0	-29.4	-	-	0.0207	0.0163	0.107	0.0746
No. 3	Mono.	38.1	-	0.0179	0.0251	-	-	-	-
	S.I.1	38.9	-36.6	-	-	0.0159	0.0209	0.0348	0.0164
	S.I.2	38.4	-37.1	-	-	0.0334	0.0375	0.0482	0.0386
	C.A.2	39.2	-37.2	-	-	0.0163	0.220	0.0372	0.0289
	C.A.3	36.6	-37.1	-	-	0.0207	0.0163	0.0494	0.246
	N.F.	36.3	-37.1	-	-	0.0234	0.0167	0.0300	0.0100

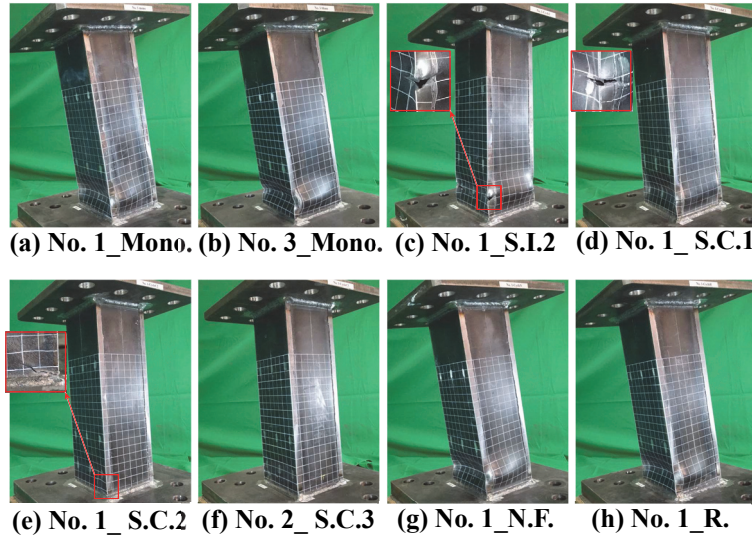
## Test results

Table 5 lists the results of the bending shear tests, and Fig. 4 shows the bending moment-rotation relationship for each loading protocol.  $\Sigma\theta_{max}^+$  and  $\Sigma\theta_{max}^-$  in Table 5 represent the cumulative plastic rotation when the ultimate strength is reached on the positive and negative sides, respectively.  $\theta_u$ ,  $\Sigma\theta_u^+$ , and  $\Sigma\theta_u^-$  are the plastic rotation and their cumulative amounts at the point where the strength reaches  $M_p$  again due to deterioration after the ultimate strength. These are calculated by removing the elastic rotation component from the bending moment-accumulated rotation relationship. In Fig. 4, the vertical axis is normalized by the full plastic moment  $M_p$ , and the horizontal axis is the rotation  $\theta$  or normalized it by the elastic rotation  $\theta_p$ , depending on the loading protocol. Figure 5 shows the collapsed mode of the specimen after loading.

First, the rotation  $\theta_{max}$  at the ultimate strength confirmed in the monotonic loading were 0.0239 rad, 0.0192 rad, and 0.0179 rad for No. 1, No. 2, and No. 3, respectively, and local buckling occurred immediately before or at the ultimate strength was reached. As shown in Figs. 5(a) and (b), the local buckling deformation formed  $0.4b$  away from the end plate, and the difference in width-to-thickness ratio had no effect on the location of local buckling. In the specimens subjected to cyclic loading, local buckling occurred when the rotation reached  $\theta_{max}$ , which is the rotation at ultimate strength during the monotonic loading, and then the strength deteriorated. In the case of incremental cyclic loading as shown in Figs. 3(b) and (c), no local buckling or associated strength deterioration occurred when the maximum amplitude of a given loop was below the rotation  $\theta_{max}$ , but as the protocol progressed and the rotation exceeded  $\theta_{max}$ , local buckling occurred at the same location as during monotonic loading and strength deterioration occurred. In these cases, ductile cracks appeared along the welding line between the web and flange in the cross-section where local buckling occurred, and the strength deteriorated further as the cracks propagated. Similarly, under the constant amplitude loading of  $\pm 0.033$  rad shown in Fig. 4(d), No. 1 experienced the amplitude exceeding the rotation  $\theta_{max}$  ( $= 0.0233$  rad), resulting in local buckling around  $0.0233$  rad and ductile crack growth on the welding line between the web and flange. In Fig. 4(e), the constant amplitude loading of  $0.020$  rad caused local buckling and significant strength deterioration due to this for No. 3, but in No. 1, since the rotation was almost equal to the  $\theta_{max}$ , local buckling occurred slightly; however, strength deterioration was not significant. Then, ductile cracks occurred at the welds between the flange and end plates, and the strength gradually deteriorated. In the case of the constant amplitude loading of  $\pm 0.015$  rad shown in Fig. 4(f), local buckling did not



**Figure 4 Comparison of moment–rotation relationships changing according to loading protocol**



**Figure 5 Failure modes under various loading protocols**

occur in No.1 and No.2 even after multiple cycles because the loading amplitude was smaller than  $\theta_{\max}$ . At this time, a slight ductile crack was observed at the welding line between the flange and end plate, and it was considered that the crack would propagate due to continuous loading. However, since the purpose of this study is to confirm the strength deterioration behavior due to local buckling, loading was terminated after 50 cycles. From these results, it is predicted that the ultimate state of a member is determined by ductile cracking rather than local buckling when subjected to constant amplitude loading with a rotation smaller than  $\theta_{\max}$ . The results when asymmetric Near-Fault type protocol was given are shown in Fig. 4(g). In this protocol, the specimen is initially subjected to a large amplitude in one direction followed by small amplitude loops; however, the specimen in No. 1 reaches the full plastic moment even when subjected to a large amplitude in the opposite direction after experiencing them. On the other hand, in the specimen No. 3, strength deterioration progressed at the time of the first large amplitude deformation, and the strength below the full plastic moment. As a result, the full plastic moment was not reached for the subsequent large amplitude in the opposite direction. Fig. 4(h) compares the result of the Ratcheting-type loading protocol (solid line) with these of monotonic loading (dashed line). Although the deterioration behavior in both cases is roughly similar, the strength deterioration under ratcheting-type loading gradually becomes steeper than monotonic as the deformation increases. It is expected that this is due to the fact that the amount of accumulated strain up to the same rotation is larger in the case of the Ratcheting-type loading.

## SIMULATION OF EXPERIMENTS BY FEM ANALYSIS

### Overview of monotonic/cyclic coupon test

Although structural experiments were conducted in the previous chapter using member geometry and loading protocol as variables, the factors affecting the structural performance of members subjected to actual bending shear are diverse, and it is difficult to exhaustively study the relevant variables by experiment. Realistically, it is essential to study this through complementary simulations using FEM analysis or other methods. On the other hand, in FEM analysis of a member subjected to cyclic loading, the elasto-plastic behavior is greatly affected by the material constitutive model of the steel, so it is necessary to set-up an elasto-plastic constitutive model that correctly reflects the characteristics of the steel. In this section, monotonic/cyclic uniaxial coupon tests are conducted prior to the numerical analysis of members. The coupon test results are used to calibrate the parameters required for the material constitutive model that combines isotropic and nonlinear kinematic hardening law, such as the Chaboche model and the Subloading surface model. These parameters will be used in the next chapter in the analysis that simulates the experiment.

Fig. 6 shows the specimen used in the uniaxial coupon test. The steel is made of the 550 N/mm<sup>2</sup> grade (Gr. 55) same as the experiments described in the prior chapter. The *Japanese Industrial Standards* (JIS) No. 5 specimen shown in Fig. 6(a) is used for the monotonic coupon test, and the circular specimen with test section dimensions of 3 mm in diameter and 7 mm in length, shown in Fig. 6(b), is used for the cyclic test. The sectional center of the circular specimen is fabricated to match the center of the plate thickness. Both specimens are machined from steel plates as shown in Fig. 6(c) so that the axial strain direction of the specimens coincided with the length direction of the member. In the monotonic coupon tensile test, the nominal strain  $\varepsilon_{eng}$  is measured by strain gauges attached to both sides of the center of the specimen. In the cyclic coupon test, the nominal strain at the center of the specimen is measured by the displacement meter capable of measuring the strain between 3 mm reference points. The loading protocol of the cyclic loading is divided into two patterns: Type A is a positive-negative cyclic type (+0.25 %, -0.25 %, +0.50 %, -0.50 %, +0.75 %, -0.75 %, +1.00 %, -1.00 %, +2.00 %, -2.00 %, +3.00 %, -3.00 %, ..., in nominal strain with the tensile side positive), and Type B is a ratcheting type (+1.50 %, +0.50 %, +2.00 %, +1.00 %, +2.50 %, +1.50 %, +3.00 %, +2.00 %, +3.50 %, +2.50 %, ...).

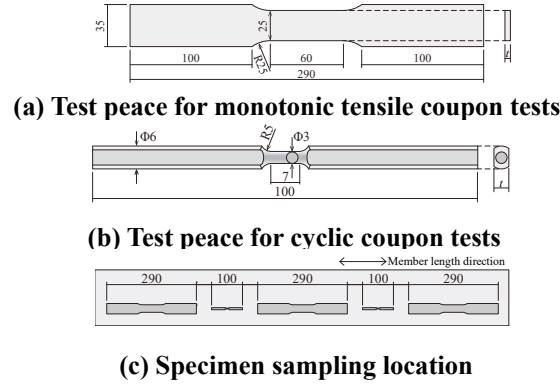


**Figure 6 The nominal dimensions of monotonic and cyclic coupons**

### Relationship between coupon test and material constitutive models

The material constitutive models available in the general-purpose analysis program MSC. Marc Mentat 2021 include the Chaboche model and the Subloading surface model. In this study, these two models are applied to the elasto-plastic numerical analysis of box-section members, and parameter calibration by uniaxial coupon tests is performed in this section. First, a brief description of each model is given. The Chaboche model is classified as a type of nonlinear kinematic hardening model that expresses the hardening characteristics of the material in the plastic range by a change of state of a single yield surface, especially by a nonlinear shift of the center point. However, it is usually used in combination with the isotropic hardening law that expresses cyclic hardening. In the case of uniaxial loading, the functions expressing the isotropic hardening and the kinematic hardening of the Chaboche model used in this paper are expressed by Eqs. (1) and (2), respectively.

$$\text{Isotropic hardening/softening} \quad R = R_{\infty}(1 - e^{-b\varepsilon^{pl}}) \quad (1)$$

$$\text{Nonlinear kinematic hardening} \quad \dot{X} = \left[ \frac{c}{R+k} (\sigma - X) - \gamma X \right] \dot{\varepsilon}^{pl} \quad (2)$$



$R_\infty$  in Eq. (1) is the stress due to isotropic hardening,  $R_\infty$  and  $b$  are the material parameter related to the isotropic hardening, and  $\varepsilon_{pl}$  is the plastic strain.  $R_\infty$  determines the limit of isotropic hardening/softening. In Eq. (2),  $X$  is the back stress component defined by Armstrong et al. (1966),  $C$ ,  $k$ , and  $\gamma$  are material parameters, and  $\gamma = 0$  means linear kinematic hardening. In the Chaboche model, a total of 7 material parameters ( $E$ ,  $\sigma_y$ ,  $R_\infty$ ,  $b$ ,  $C$ ,  $k$ ,  $\gamma, \eta$ ) are subject to calibration. The steel used in this paper does not exhibit isotropic softening, so parameter  $k$  becomes to 0. The Subloading surface model is also a material constitutive model proposed to improve the accuracy of simulating material nonlinearity, including the case of cyclic loading. A unique feature of this model is its ability to follow the continuous change in stress gradients (smoothness condition) from the elastic to plastic range. In the classical elasto-plastic model represented by the Chaboche model, the plastic strain does not occur until the stress level reaches the yield surface, thus resulting in a discontinuous change in stress gradient before and after yielding. On the other hand, in the stress-strain relationship of actual steel, the elastic modulus decreases in stages and plastic strain accumulates before the stress reaches a certain yield condition. The Subloading surface model can simulate this smooth variation in stress gradient by defining a subloading surface that represents the elastic limit further inward than the yield surface. The functions of the Subloading surface model used in this paper are expressed from Eq. (3) to (10).

$$f(\hat{\sigma}) = RF(H) = \sqrt{3/2}R\|\hat{\sigma}\| \quad (3)$$

$$\hat{\sigma} = \sigma - \alpha \quad (4)$$

$$d\alpha = c_k(d\varepsilon^{pl} - \frac{1}{\sqrt{3/2}\zeta F}\|d\varepsilon^{pl}\|\alpha) \quad (5)$$

$$\dot{F} = F_0 h_1 h_2 e^{-h_2 H} \quad (6)$$

$$dH = \sqrt{2/3}\|d\varepsilon^{pl}\| \quad (7)$$

$$dR = U(R)\|d\varepsilon^{pl}\| \quad (8)$$

$$U(R) = u \cot \left[ \frac{\pi}{2} \left( \frac{R-R_e}{1-R_e} \right)^n \right] \quad (9)$$

$$u = \bar{u} e^{-u_c R_c C \sigma} \quad (10)$$

$R$  in Eq. (3) is called the normal yield ratio and is the ratio of the size of the subloading surface to the yield surface. The gap between these yield surfaces causes a reduction in the elastic modulus at an early stage.  $F$  is the hardening function with the isotropic hardening variable  $H$  as an argument, expressed by the initial yield stress  $F_0$  and the material parameters  $h_1$  and  $h_2$ .  $\alpha$  is the kinematic hardening variable, determined by the material parameters  $c_k$  and  $\zeta$ .  $U$  is a monotonically decreasing function with respect to  $R$ , determined by the  $R$  and the function  $u$  consisting of the material parameters  $\bar{u}$  and  $u_c$  shown in Eq. (10). As shown in Eq. (10),  $u$  includes the material constants  $R_c$  and  $C$  as factors, but since these parameters are not involved in this paper. Therefore, the Subloading surface model performs the calibration work for all 9 parameters ( $E$ ,  $\sigma_y$ ,  $h_1$ ,  $h_2$ ,  $c_k$ ,  $\zeta$ ,  $R_e$ ,  $\bar{u}$ ,  $u_c$ ).

### Simulation of coupon tests using material constitutive models

Fig. 7 shows the nominal stress ( $\sigma_{eng}$ ) - nominal strain ( $\varepsilon_{eng}$ ) relationship based on monotonic/cyclic coupon test results. In Protocol Type A, buckling occurred in the test section at a strain of about -4.0% on the compression side, so the results up to -3.0% are shown. As shown in Fig. 7, the results of the monotonic test generally agree with the Type B envelope curve. In Type A, cyclic hardening can be observed as the cycles progress. The material parameters shown in the previous section are calibrated for the cyclic test results shown in Fig. 7. As shown in Eq. (11), the sum of the squared difference between the stress degree  $\sigma_{EXP}$  obtained from the coupon test and the stress  $\sigma_{CONS}$  simulated by each constitutive model is set as the objective function  $j$ . For each model, the set of parameters that minimizes this objective function is calculated using the differential evolution method. In the calibration process, the entire test data is decomposed into multiple monotonic histories, where  $N$  in Eq. (11) represents the total number of measured points and  $N_r$  represents the number of points in the  $r$ -th process. When using cyclic test results, the first loop determines the initial stiffness of the material and also corresponds to the strain level at which buckling deformation occurs in the member. Therefore, as the accuracy of this first loop is emphasized, the evaluation value of the first loop is set to have the same weight as all subsequent loops in the objective function  $j$ . The parameters calibrated for each steel grade and loading protocol are shown in Table 6.

$$j = \frac{1}{N} \left[ \frac{N - N_1}{N_1} \sum_{r=1}^1 \sum_{n=1}^{N_r} (\sigma_{EXP,r,n} - \sigma_{CONS,r,n})^2 + \sum_{r=2}^R \sum_{n=1}^{N_r} (\sigma_{EXP,r,n} - \sigma_{CONS,r,n})^2 \right] \quad (11)$$

Fig. 8 compares the coupon tests of 550 N/mm<sup>2</sup> grade steel ( $t=4.5\text{mm}$ ) with the FEM simulation conducted in this section. The FEM analysis is based on a 1 mm cubic model consisting of a single solid element with no expansion deformation constraints. For all simulations, including the following section, the FEM analysis program MSC. Marc Mentat 2021 is used in this study. The circle plot shows the experimental results. The solid green and dashed green lines are the results of the isotropic or linear kinematic hardening law. Model parameters are calibrated by fitting the true stress-plastic strain relationship of the monotonic coupon test results with each law. The red line and blue line are simulated by the Chaboche model and the Subloading surface model, respectively. The result of simulating by the isotropic hardening law only (green solid line), is significantly different from the test result, in which the stress is overestimated with respect to the progress of plastic strain. When applying the linear kinematic hardening law only (green dashed lines), the accuracy of the tensile stress side of Type B shown in Fig. 8(b) is high; however, the compressive stress side of Type B and Type A are under-stressed compared to the coupon test results. In addition to the above, the accuracy of the Bauschinger part is not sufficient in these cases, and it can be said that the isotropic hardening law and the linear kinematic hardening law are difficult to simulate the cyclic coupon test with high precision. The Subloading surface model (blue line) and Chaboche model (red line) simulate the stress increase due to isotropic hardening and the behavior in the Bauschinger part through Types A and B, which is better accuracy than when isotropic or linear kinematic law. In these models, the accuracy deteriorate in the Bauschinger part on the tensile stress side; however, this is due to the priority is given to the accuracy of the initial loop during optimization. As shown in Table 6, the yield stress (initial yield surface) calibration results for the Chaboche model are lower than those obtained from the monotonic coupon test, and the accuracy of the first loop of Type B in Fig. 8 is less accurate than that of the Subloading surface model.

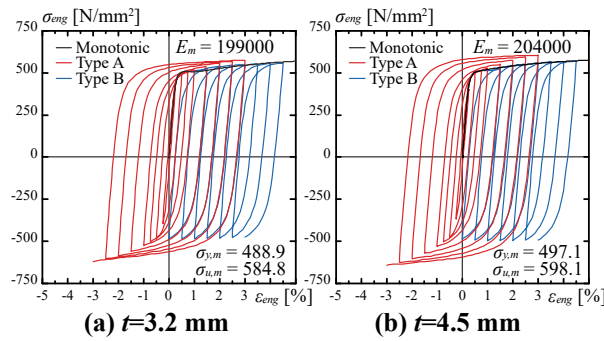


Figure 7 Coupon test results

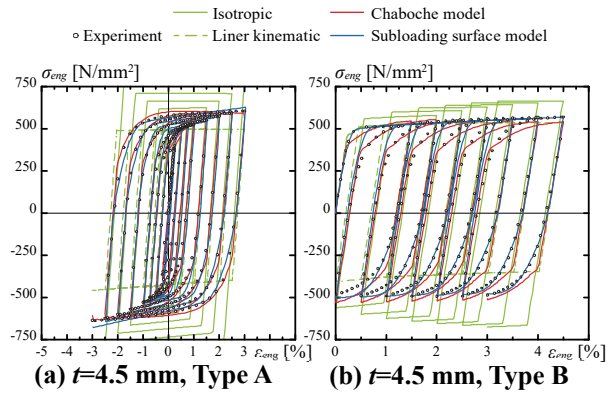


Figure 8 Comparison of coupon test and FEM simulation

Table 6 Calibration results for chaboche and Subloading surface model

Grade	$t$	Loading type	Chaboche model							Subloading surface model								
			$E$	$\sigma_y$	$R_\infty$	$b$	$C$	$\gamma$		$E$	$\sigma_y$	$h_1$	$h_2$	$c_k$	$\zeta$	$R_e$	$\bar{u}$	$u_c$
Gr. 55	3.2	A	205000	339.0	42.55	88.83	33200	289.3		209000	507.1	2.720	0.616	1353.2	0.153	0.678	305.1	5.348
		B	189000	411.9	28.06	57.53	15847	81.9		197000	510.7	0.0259	51.46	903.1	0.511	0.322	156.4	6.019
	4.5	A	194000	333.4	41.52	287.75	34772	244.9		204000	490.9	0.5034	8.471	1403.5	0.540	0.409	732.4	5.126
		B	211000	368.3	38.43	210.3	30016	230.6		210000	510.7	0.0592	20.99	1401.6	0.492	0.046	742.9	6.310

## Relationship between the results of bending shear experiments and the material constitutive model

In this section, the calibrated material parameters are used for the simulation of the experiments in the previous chapter. Fig. 9 shows the FEM analysis model. Each plate surface is divided into 20 equal sections in its width direction, and the range from bottom edge to plate width  $b$  in the length direction is also divided with the same mesh size. To reduce the analytical load, the direction of the material length, from the section width  $b$  to the loading position, the division is progressively coarser so that the maximum element length is about five times larger than the minimum element length. The plate thickness direction is divided into two elements. Note that welding is not reproduced in this analysis. As boundary conditions, displacement and rotation are constrained at the bottom end, and out-of-plane displacement and torsional deformation are constrained at the upper end. The upper end is tethered by a rigid link element to a reference point A placed at the center of the section, giving the same loading protocol to reference node A as in the experiment. The material properties are the Chaboche and Subloading surface model shown in Table 6. In addition to these, isotropic and kinematic hardening laws based on monotonic coupon tests are also considered. The initial imperfection is installed based on the first eigenmodes and its maximum amplitude is 1/2000 of the section width.



Fig. 11 shows the results of structural tests and FEM analysis. The results are shown here for No. 1 and No. 3, which have the smallest and largest width-to-thickness ratios, and for monotonic and Near-Fault type cyclic loading as the protocol. As shown in Fig. 11(a), the Chaboche model simulates similar values for ultimate strength as in the experiment; however, the rotation at the ultimate strength is larger than in the experiment because of earlier nonlinearization and slower load increase. Although the Chaboche model has relatively good accuracy for the cyclic coupon test shown in Fig. 8, the calibration result of the initial yield stress  $\sigma_y$ , shown in Table 6 is about 30% lower than the monotonic test result. This results in a less accurate simulation of the first loop of the cyclic coupon test shown in Fig. 8, and the above results can also be attributed to this lower  $\sigma_y$ . On the other hand, the simulated results of monotonic tests with the Subloading surface model are almost the same as those with the isotropic and linear kinematic hardening law. In the Subloading surface model, the elastic modulus decreases early in response to deformation due to the nature of the model, which assumes a plastic state even before the initial yield stress level  $\sigma_y$  is reached. This results in an earlier stiffness decline under monotonic loading than in the experiment, but better accuracy is obtained with parameters optimized from the coupon test results with Type B. The results for the Near-Fault type, show a marked difference between the Chaboche and the Subloading surface model and the other two. When the isotropic hardening rule is applied (solid green line), the excessive cyclic hardening causes elastic behavior even at amplitudes where plasticization would have progressed in the experiment, resulting in deteriorated accuracy, and errors in the Bauschinger part are also noticeable. When the linear kinematic law is applied (green dashed line), strength and stiffness decrease at an early stage, and although this is a safer simulation, its accuracy is inadequate. The Subloading surface model and the Chaboche model show good agreement with the experimental results in terms of the deterioration behavior of strength as the loading protocol progresses. Although some deviations are observed in the behavior of the Bauschinger part, the accuracy is higher than that of the results obtained using other models. Fig. 10 shows the local buckling deformation observed when the Near-Fault type is applied to No. 3. The deformations shown in the figure are at the red circle in Fig. 11(d), and are in the deteriorated strength region. It is confirmed that the deformation of local buckling is simulated as in the experiment by using the Chaboche model and the Subloading surface model.

In conclusion, in the simulation analysis of box-section members subjected to monotonic loading, although there is some early stiffness reduction when the Subloading surface model is applied, but there is no significant difference between the results when the isotropic hardening law or the linear kinematic hardening law is applied. Here, a slightly larger error in deformation is observed only when the Chaboche model is applied. On the other hand, when simulating cyclic deformation behavior, isotropic/kinematic hardening only does not provide hardening, such as the Chaboche model or the Subloading surface model. It should be noted, however, that the Chaboche model, tends to result in initial yield surfaces that are smaller than the actual yield stress of the steel and may underestimate the member strength.

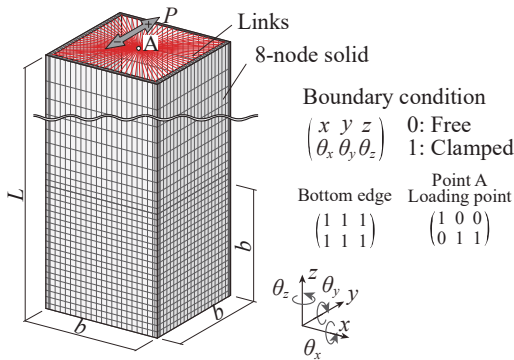


Figure 9 FEM analysis model of box-section column

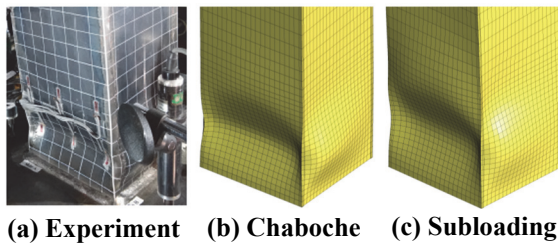


Figure 10 Simulated and experimentally obtained deformation profiles (No. 3, L.P.: Near-Fault)

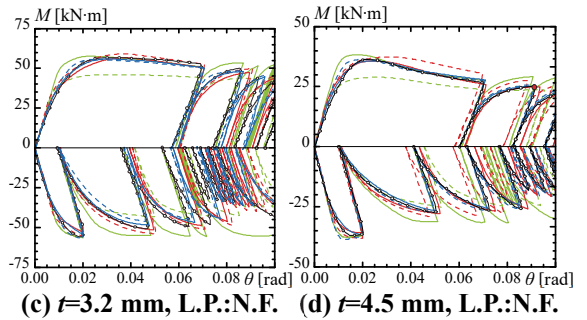
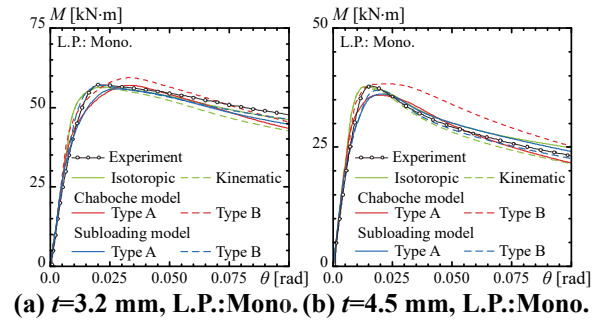


Figure 11 Comparison of column test and FEM simulation

## CONCLUSION

In this study, we experimentally analyzed the effects of the cyclic loading protocol on the structural performance determined by the local buckling of welded box-section members. In addition, simulation analysis by FEM using various constitutive models was conducted to examine the accuracy and applicability of each model. In a specimen subjected to incremental cyclic loading, local buckling and ductile cracking on the web-flange joint line occurred only when the maximum rotation of a loop exceeds the rotation  $\theta_{\max}$  at ultimate strength under monotonic loading, thereby reducing the load capacity. Similarly, in constant amplitude loading, if the loading amplitude is below  $\theta_{\max}$ , no buckling or resulting strength deterioration occurs. In such cases, ductile cracks appear at the welds between the flange and end plate, which is considered to determine the ultimate state. In the FEM analysis of the box-section members subjected to monotonic loading, the accuracy of the Subloading surface model was slightly better in terms of initial stiffness; however, the difference from the results obtained by applying the isotropic/linear kinematic hardening law, whose parameters were defined from the monotonic coupon test, was small. The Chaboche model characteristically requires an excessively small value of yield stress to reproduce the Bauschinger part, which may lead to poor accuracy during member-scale analysis. In cyclic loading, it is difficult for isotropic/linear kinematic laws to accurately simulate experiments, and it is useful to apply combined hardening law with nonlinear kinematic hardening, such as the Chaboche model or the Subloading surface model.

## REFERENCES

- Architectural Institute of Japan, *Recommendation for Limit State Design of Steel Structures*, 2010 (in Japanese)
- Armstrong, P.J., Frederick, C.O., “A mathematical representation of the multiaxial Baushinger effect”, GEGB report RD/B/N731, Berkley Nuclear Laboratories, 1966
- Chaboche, J.L., Rousselier, G., “On the Plastic and Viscoplastic Constitutive Equations–Part I: Rules Developed With Internal Variable Concept”, *ASME Journal of Pressure Vessel Technology*, Vol. 105, Issue. 2, pp. 153–158, 1983. 5,
- Hashiguchi, K., “Subloading surface model in unconventional plasticity”, *International Journal of Solids and Structures*, Vol. 25, Issue 8, pp. 917–945, 1989
- Kurata, M., Nakashima, M., Suita, K., “Test on Large Cyclic Deformation of Steel Tube Columns Having Fixed Column Bases”, *Journal of Structural and Construction Engineering*, Vol. 70, No. 598, pp. 149–154, 2005. 3 (in Japanese)
- Murakami, R., Koetaka, Y., “Deteriorating Behavior due to Local Buckling and Fracture of H-shaped Steel Beam with Axial Deformation Restriction”, *Journal of Structural and Construction Engineering*, Vol. 83, No. 748, pp. 913–921, 2018. 6 (in Japanese)
- Sato, A., Mitsui, K., “Experimental Study on Square Steel Tubular Columns under Compressive Axial Force with One End Cyclic Bending Moment”, *Journal of Structural and Construction Engineering*, Vol. 82, No. 735, pp. 701–711, 2017. 5 (in Japanese)
- Sato, K., Ikarashi, K., “Local Buckling Behavior and Evaluation Method for Structural Performance of Square Hollow Section Members under Bending Shear Force”, *Journal of Structural and Construction Engineering*, Vol. 82, No. 731, pp. 123–133, 2017. 1 (in Japanese)
- Suzuki, Y., Lignos, D.G., “Experimental Evaluation of Steel Columns under Seismic Hazard-Consistent Collapse Loading Protocols”, *Journal of Structural Engineering*, Vol. 147, Issue 4, 2021. 4
- Tsuda, K., Matsui, C., “Strength of Square Steel Tubular Beam-Columns under Constant Vertical and Horizontal Loads”, *Journal of Structural and Construction Engineering*, No. 512, pp. 149–156, 1998. 10 (in Japanese)
- Yamada, S., Ishida, T., Shimada, Y., “Hysteresis Model of RHS Columns in the Deteriorating Range Governed by Local Buckling”, *Journal of Structural and Construction Engineering*, Vol. 77, No. 674, pp. 627–636, 2012. 4 (in Japanese)
- Yoshida, F., Umemori, T., “A model of large-strain cyclic plasticity and its application to springback simulation”, *International Journal of Mechanical Sciences*, Vol. 45, Issues 10, pp. 1687–1702, 2003. 10